Reluctance Force Magnetic Suspension Characteristics and Control for Cylindrical Rotor Bearingless Motors

Citation: Zhou, Lei, and David L. Trumper. "Reluctance Force Magnetic Suspension Characteristics and Control for Cylindrical Rotor Bearingless Motors." Journal of Dynamic Systems, Measurement, and Control 139, 3 (January 2017): 031003 © 2017 ASME

As Published: http://dx.doi.org/10.1115/1.4035007

Publisher: ASME International

Persistent URL: http://hdl.handle.net/1721.1/120035

Version: Final published version: final published article, as it appeared in a journal, conference proceedings, or other formally published context

Lei Zhou
Department of Mechanical Engineering,
Massachusetts Institute of Technology,
Cambridge, MA 02139
e-mail: leizhou@mit.edu

David L. Trumper
Professor
Mem. ASME
Department of Mechanical Engineering,
Massachusetts Institute of Technology,
Cambridge, MA 02139
e-mail: trumper@mit.edu

Reluctance Force Magnetic Suspension Characteristics and Control for Cylindrical Rotor Bearingless Motors

In this paper, the modeling and control of reluctance-force-based magnetic suspension in cylindrical rotor, smooth air-gap bearingless motors are presented. The full suspension system dynamics, including both the destabilizing forces due to the motor field and the active magnetic suspension control forces, are modeled, and a transfer function of the bearingless motor suspension plant is derived. It is shown that the suspension system dynamics in a bearingless motor depend on the motor winding current amplitude. This requires the magnetic suspension controllers to address the changing system dynamics and to stabilize the suspension under different driving conditions. A controller design with its gains changing with the motor winding current amplitude is proposed. The derived model and the proposed controller design are verified by experiments with a hybrid hysteresis–induction type bearingless motor. It is shown that the derived mathematical model provides an effective basis for loop-shaping control design for the reluctance-force-based magnetic suspension systems in bearingless motors, and the proposed controller design can stabilize the rotor's suspension under varying excitation conditions. [DOI: 10.1115/1.4035007]

1 Introduction

In the past decades, there has been significant development in the area of bearingless drive technology. The bearingless motor has many distinct advantages. As with other types of magnetic bearings, the bearingless motors can eliminate mechanical friction, vibrations, and lubrication in mechanical bearings, which makes them attractive for precision and in-vacuum applications. Besides, compared with other magnetic bearing technologies, the bearingless motor has the advantage of compactness, and this feature allows them to be used in small devices [1]. It also allows velocity and position control, so that this motor and bearing concept can be widely used in servo-control applications [2].

The bearingless motors can be roughly categorized by their motor principles, such as bearingless permanent magnet (PM) motors [3–5], bearingless induction motors [6], bearingless reluctance motors [7], and bearingless hysteresis motors [8,9]. Among many different types of bearingless motor, the cylindrical rotor (no salient poles) bearingless motors with reluctance-force-based magnetic suspension are the most basic kind. In these motors, the magnetic reluctance forces between the stator and the rotor provide the dominant radial forces for magnetic suspension, and the effect of the rotor field is small compared to that of the reluctance forces. In this category, there are bearingless hysteresis motors with highly permeable rotors [8,9], bearingless solid rotor induction motors with sheet conductor and back iron in rotors [10], and general bearingless induction motors under no-load condition [11]. The reluctance force magnetic suspension also forms a primitive for other types of bearingless motors [12].

Similar to other magnetic suspension systems, the reluctance force magnetic suspension in a bearingless motor has unstable dynamics when in open-loop. Typically, a bearingless motor has two sets of windings, called motor windings and suspension windings, arranged in the stator. The motor windings generate a rotating magnetic field for torque generation and also produce destabilizing radial forces, which make the rotor open-loop unstable at the center position. On top of the motor field, another magnetic field generated by the suspension windings interacts with the motor field and generates suspension control forces. Both these magnetic fields will influence the rotor's dynamics in the radial directions, and a complete model for the rotor's dynamics is necessary for understanding the system behavior and for suspension controller synthesis.

Through the years, there have been many studies modeling the reluctance force magnetic suspension in bearingless motors. The radial suspension force generation in general bearingless alternating current (AC) motors has been modeled in Ref. [13] and later in Ref. [12], where the suspension forces are calculated by means of magnetic energy. Later work [14] analyzes the suspension force generation with the rotor eccentricity taken into consideration, and a bearingless induction motor with suspension force feedback has been studied in Ref. [15]. However, to the best of our knowledge, the modeling of the plant dynamics of the magnetic suspension in a PM-less bearingless motor, including the destabilizing radial forces induced by the motor field, has not yet been reported in the literature.

In this paper, an analytical model of the reluctance force radial magnetic suspension in a cylindrical rotor bearingless motor is derived based on the fundamental electromagnetics, and a transfer function model for the suspension system is derived. The model is validated through experiments with a hybrid hysteresis–induction type bearingless motor, which is an AC motor with a solid rotor made of D2 steel. The loop-shaping method is applied for the suspension compensator design, and a controller with its gains varying with the motor winding current amplitude is proposed. The test results show that the proposed controller design can stabilize the suspension system under varying excitation conditions.

The remainder of this paper is organized as follows: The operating principles of the reluctance force magnetic suspension in a bearingless motor are briefly introduced in Sec. 2. The mathematical model of the magnetic suspension system dynamics is derived in Sec. 3. The experimental validation for the derived model is presented in Sec. 4, and the suspension controller design and tests are introduced in Sec. 5. Conclusions are presented in Sec. 6.

Contributed by the Dynamic Systems Division of ASME for publication in the JOURNAL OF DYNAMIC SYSTEMS, MEASUREMENT, AND CONTROL. Manuscript received April 18, 2015; final manuscript received October 11, 2016; published online January 10, 2017. Assoc. Editor: Azim Eskandarian.

2 Operating Principle

In a bearingless motor, the reluctance-force-based magnetic levitation of the rotor is achieved by arranging two sets of windings in the stator slots. One set of windings has P poles, which are used for motor torque production. The other set of windings has $P \pm 2$ poles, which are used for the radial suspension force generation. These two windings are called motor windings and suspension windings, respectively. Figure 1 shows a schematic diagram of the multiple-winding-type cylindrical rotor bearingless motor. Two sets of two-phase windings are wound on the stator: the four-pole windings are 4*a* and 4*b*, and the two-pole windings are 2*a* and 2*b*. The positive current directions in the windings are shown by the crosses and the dots. In this discussion, we assume that the four-pole windings are the motor windings, and the two-pole windings are the suspension windings.

When the motor windings are excited with symmetric AC currents, and no current is flowing in the suspension windings, a rotating four-pole magnetic field is produced in the motor. The four-pole field lines (solid) in Fig. 1 show the motor magnetic field at a time instant when the four magnetic poles are aligned with the x- and y-axes. Under this condition, if the rotor is centered, the magnetic flux density in the air gaps 1 and 3 in Fig. 1 is equal, and no net radial force is generated on the rotor in the x-direction.

Under the same current conditions as before, let us slightly perturb the rotor's position toward the negative x-direction in Fig. 1. In this case, the magnetic field in the air gap 3 becomes stronger than the magnetic field in the air gap 1. As a result, there will be a net force in the negative x-direction acting on the rotor, and this force increases as the rotor eccentric displacement grows. This indicates that the rotor is open-loop unstable at the center bore of the stator under applied motor fields, and feedback control is necessary to stabilize the magnetic suspension of the rotor.

On top of the four-pole motor field, when we excite the suspension winding 2*a* with a positive current, the two-pole magnetic field line as is shown in Fig. 1 (dashed) is produced. Under this circumstance, the magnetic flux density is increased in the air gap 1 and is decreased in the air gap 3. This unbalanced air-gap flux density generates magnetic reluctance forces in the two air gaps, and a total force in the positive x-direction is generated on the rotor, which can accelerate the rotor in the x-direction. Similarly, with a current in the 2*b* winding, a y-direction control force can be generated. From this discussion, one can see qualitatively that the bearingless motor is a *flux steering* device [16], where the two-pole magnetic field is interacting with the four-pole motor field to produce radial suspension forces.

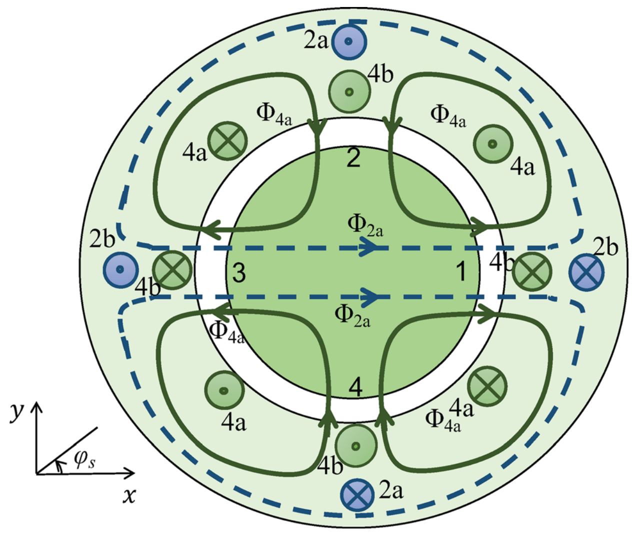

Fig. 1 Winding arrangement in a bearingless motor assuming a two-phase configuration. Here, the four-pole windings 4*a*, 4*b* are the motor windings, and the two-pole windings 2*a*, 2*b* are the suspension windings.

3 Bearingless Motor Modeling

In this section, the dynamics of the reluctance force magnetic suspension in a bearingless motor are modeled. We extended the analysis in Ref. [13] by including the destabilizing forces generated by the motor field, and derive a transfer function model for the bearingless motor suspension system.

3.1 Air-Gap Variation and Magnetic Circuit Model.

Figure 1 shows a diagram for the motor being analyzed. Here, the two-phase windings are assumed for simplicity. The analysis can be readily transformed into a three-phase system by means of Clarke transformations [17]. The following analysis is based on a sinusoidal distribution assumption of the stator magnetomotive force (MMF). The higher-order harmonics and saturation effects are neglected. The perpendicular axes x and y are fixed to the stator. Define the instantaneous currents that flow in the windings 4*a*, 4*b*, 2*a*, and 2*b* as i_{4a}, i_{4b}, i_{2a}, and i_{2b}, respectively. N_4 and N_2 are the number of turns per phase per pole for the four-pole and two-pole windings, respectively.

Figure 2 shows a diagram of the MMF generated by the full pitch, concentrated winding 2*a* and its associated fundamental component. Here, the horizontal axis corresponds to the angular coordinate ϕ_s in Fig. 1, which is a counterclockwise angular position starting from the x-axis. The positive direction of MMF is defined in the radial direction from the rotor to the stator. With concentrated conductors 2*a* at $\phi_s = \pi/2$ and $3\pi/2$, the corresponding MMF distribution is a square wave of amplitude $N_2 i_{2a}/2$. By neglecting all higher-order harmonics of this MMF wave and only considering its fundamental component, the magnitude of the approximating sinusoidal MMF wave is $2N_2 i_{2a}/\pi$. Similarly, the fundamental harmonics of the MMF distributions for the four windings are

$$\Theta_{4a} = \frac{2}{\pi} N_4 i_{4a} \cos 2\phi_s \tag{1}$$

$$\Theta_{4b} = \frac{2}{\pi} N_4 i_{4b} \sin 2\phi_s \tag{2}$$

$$\Theta_{2a} = \frac{2}{\pi} N_2 i_{2a} \cos \phi_s \tag{3}$$

$$\Theta_{2b} = \frac{2}{\pi} N_2 i_{2b} \sin \phi_s \tag{4}$$

For distributed winding motors, the MMF can be calculated by a superposition of the MMF generated in each slot [17].

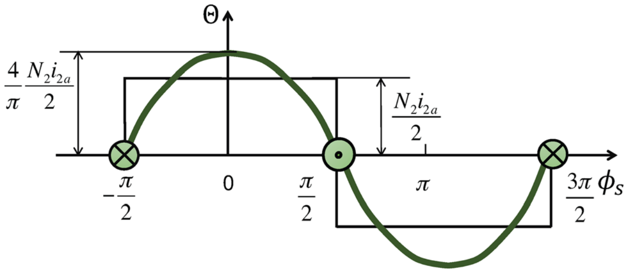

Fig. 2 The MMF distribution generated by the winding 2*a* and its associated fundamental component. The horizontal axis is the spatial angle ϕ_s. The black line shows the MMF of a concentrated winding, and the dark green line shows the fundamental component.

Figure 3 shows a diagram of air-gap length variation due to an eccentric displacement of the rotor. The x–y coordinate is fixed to the stator center. The rotor center is shown displaced in the positive direction along the two axes. Define the nominal air gap between the rotor and stator as g_0 when the rotor is centered. If the rotor's radial displacements are x and y in the corresponding directions, the air-gap length g between the rotor and the stator can then be written as

$$g(\phi_s) = g_0 - x\cos\phi_s - y\sin\phi_s \tag{5}$$

Assume the rotor displacements x and y are small compared to the nominal air-gap length g_0. The air-gap permeance P_0 at angular position ϕ_s can be calculated by ignoring second- and higher-order terms as

$$P_0(\phi_s) = \frac{\mu_0 Rl}{g} = \frac{\mu_0 Rl}{g_0}\left(1 + \frac{x}{g_0}\cos\phi_s + \frac{y}{g_0}\sin\phi_s\right) \tag{6}$$

where μ_0 is the air permeability, R is the rotor radius, and l is the motor length.

3.2 Flux Distribution. In this section, the magnetic flux distributions are calculated to find the radial forces acting on the rotor. Assume that the stator yoke is infinitely permeable with the windings on its surface, and thus, the flux distribution as a function of the angular position ϕ_s can be determined by the air-gap permeance P_0 and rotor magnetic potential with respect to the stator. When the $2a$ winding is excited by a current i_{2a}, the generated air-gap flux distribution Φ_{2a} can be written as

$$\Phi_{2a}(\phi_s) = P_0(\phi_s)(\Theta_{2a}(\phi_s) + V_{2a}) \tag{7}$$

where V_{2a} is the magnetic potential of the rotor induced by the $2a$ winding current.

According to the Gauss' law, taking a closed surface around the rotor, an integral of the flux through this surface equals zero as

$$\int_0^{2\pi} \Phi_{2a}(\phi_s)\mathrm{d}\phi_s = 0 \tag{8}$$

Substituting Eqs. (4), (6), and (7) into Eq. (8), the magnetic potential of the rotor with respect to the stator induced by winding $2a$ can be calculated as

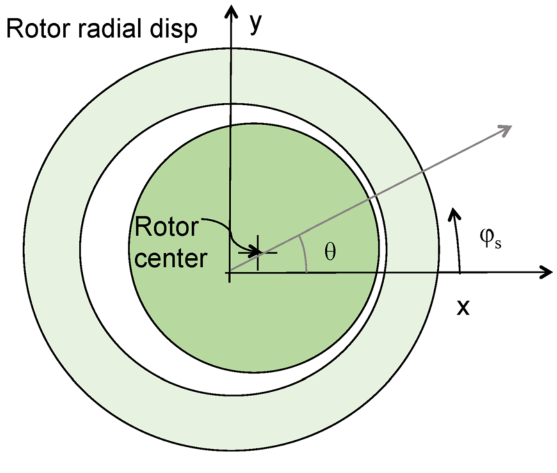

Fig. 3 Air-gap length variation with a rotor eccentric displacement to the θ-direction

$$V_{2a} = -\frac{\int_0^{2\pi} P_0\Theta_{2a}\mathrm{d}\phi_s}{\int_0^{2\pi} P_0\mathrm{d}\phi_s} = -\frac{N_2 i_{2a}}{\pi g_0}x \tag{9}$$

The above equation implies that the magnetic potential of the rotor is zero if the rotor is centered, and when there is an eccentric displacement, the magnetic potential produced by the $2a$ winding V_{2a} is proportional to the rotor displacement in the x-direction. Note that the variable y does not appear in the expression of V_{2a} under the small displacement assumption. Similarly, we can calculate the rotor magnetic potential induced by all sets of windings, $2b$, $4a$, and $4b$, as

$$V_{2b} = -\frac{N_2 i_{2b}}{\pi g_0}y \tag{10}$$

$$V_{4a}, V_{4b} = 0 \tag{11}$$

Note that the magnetic potential induced by the four-pole windings is zero.

The air-gap flux generated by winding $2a$ can be calculated by substituting Eq. (9) into Eq. (7), and the result can be written as

$$\Phi_{2a}(\phi_s) = P_0(\phi_s)\left(\Theta_{2a}(\phi_s) - \frac{N_2 i_{2a}}{\pi g_0}x\right) \tag{12}$$

Similarly, when windings $2b$, $4a$, and $4b$ are excited by the corresponding currents, the generated air-gap magnetic flux distributions are

$$\Phi_{2b}(\phi_s) = P_0(\phi_s)\left(\Theta_{2b}(\phi_s) - \frac{N_2 i_{2b}}{\pi g_0}y\right) \tag{13}$$

$$\Phi_{4a}(\phi_s) = P_0(\phi_s)\Theta_{4a}(\phi_s) \tag{14}$$

$$\Phi_{4b}(\phi_s) = P_0(\phi_s)\Theta_{4b}(\phi_s) \tag{15}$$

3.3 Negative Stiffness. When the motor is operating, the motor windings are excited with symmetrical AC currents. Under this condition, the rotor is unstable in the radial directions, since the radial forces acting on the rotor at the magnetic poles are pointing in the same direction as the rotor eccentric displacement. In this section, this destabilizing radial force is calculated, and a *negative stiffness* of the system is derived via linearizing the force with respect to the rotor displacement.

Let us assume that the two-phase AC currents in the four-pole motor windings are

$$i_{4a} = I_4\cos 2\theta, \quad i_{4b} = I_4\sin 2\theta \tag{16}$$

where I_4 is the peak amplitude for the motor currents, θ is the motor mechanical angle indicating the position of the magnetic poles, and 2θ is the corresponding electrical angle. When the motor is running, $2\theta = \omega_e t$, where ω_e is the electrical frequency of the excitation currents. The sinusoidal MMF distributions generated by these AC motor winding currents can be calculated by substituting Eq. (16) into Eq. (2). Four magnetic poles are be generated along the stator at angular positions $\phi_s = \theta$, $\theta + \pi/2$, $\theta + \pi$ and $\theta + 3\pi/4$. Unstable attractive magnetic forces between the rotor and the stator are generated at these positions, and the rotor's eccentric displacement driven by these forces is also toward one of these directions. In this analysis, let us assume that the eccentric displacement of the rotor is toward the direction of $\phi_s = \theta$ without loss of generality. Figure 4 shows a diagram of the rotor's displacement under the motor field at a time instant that $\theta = 0$. Define the rotor's displacement in x- and y-directions as

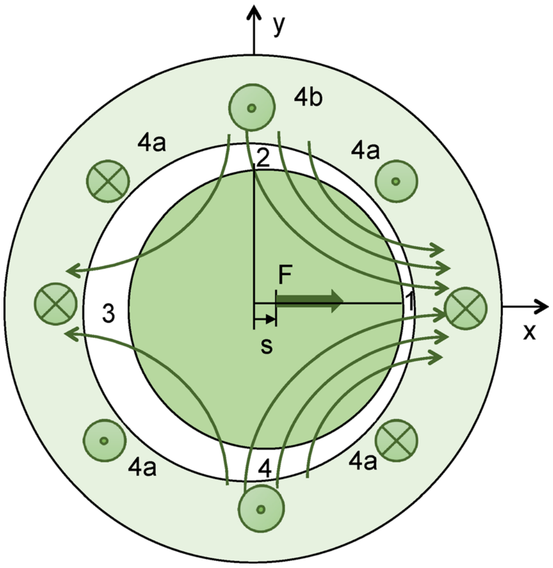

Fig. 4 Unstable radial force generation when only the four-pole motor windings are excited. Attractive forces are generated in the air gaps 1, 2, 3, and 4. The rotor has an eccentric displacement *s* in the air gap 1 direction, which induces a radial force in this direction.

$$x = s \;\cos\theta; \quad y = s \;\sin\theta \tag{17}$$

The total flux distribution generated by the four-pole windings can then be calculated by a superposition of the Φ_{4a} and Φ_{4b} that are given in Eqs. (14) and (15), respectively. Substituting Eqs. (6) and (17) into Eqs. (14) and (15), the total motor field flux distribution can be calculated as

$$\begin{aligned}\Phi_{4a4b} &= \frac{\mu_0 Rl}{g_0}\left(1+\frac{s}{g_0}\cos\theta\cos\phi_s+\frac{s}{g_0}\sin\theta\sin\phi_s\right)\\ &\quad\cdot\frac{2N_4 I_4}{\pi}(\cos 2\theta\cos 2\phi_s+\sin 2\theta\sin 2\phi_s)\end{aligned} \tag{18}$$

The destabilizing radial forces between the rotor and the stator can be calculated by means of the Maxwell stress tensor. The reluctance radial force per unit area generated by the motor field can be calculated by $\sigma_{4a4b} = B^2_{4a4b}/2\mu_0$, where B_{4a4b} is the air-gap magnetic flux density generated by four-pole motor excitations. The total radial force acting on the rotor in the direction of $\phi_s = \theta$ can be calculated as

$$f^m = \int_0^{2\pi}\frac{\Phi^2_{4a4b}}{2Rl\mu_0}\cos(\phi_s-\theta)\mathrm{d}\phi_s \tag{19}$$

Substituting Eq. (18) into Eq. (19), the radial force acting on the rotor is

$$f^m = \frac{2\mu_0 RlN_4^2 I_4^2}{\pi g_0^3}s \tag{20}$$

The above equation demonstrates the relationship between the destabilizing radial force f^m generated by the motor field only and the rotor eccentric displacement s. This relation resembles the mechanical impedance of a spring: The force is proportional to the corresponding displacement. Note here that the spring constant is negative, in that the magnetic force produced by the motor field is in the same direction as the displacement. This makes the rotor unstable at the center of the stator bore. Let us define the coefficient in Eq. (20) as the *negative stiffness* of the reluctance force magnetic suspension in a bearingless motor as

$$K_s = \frac{2\mu_0 RlN_4^2 I_4^2}{\pi g_0^3} \tag{21}$$

The radial force generated by the motor field acting on the rotor can then be written as $f^m = K_s s$.

3.4 Force Constant.

In this section, the radial suspension forces generated by the interactions between the motor windings and the suspension windings are derived. This derivation uses the Maxwell stress tensor method. Alternatively, the same result can be derived using the magnetic energy method, which has been presented in Ref. [13]. Let us first consider the suspension force generation by the interaction between the 4*a* winding and the 2*a* winding. When the 4*a* and 2*a* windings are excited with the corresponding currents i_{4a} and $i_2 a$, the total flux can be calculated by a superposition of the four-pole field and the two-pole field as

$$\begin{aligned}\Phi_{4a2a} &= \Phi_{4a}+\Phi_{2a}\\ &= P_0\left(\Theta_{4a}+\Theta_{2a}-\frac{N_2 i_{2a}}{\pi g_0}x\right)\end{aligned} \tag{22}$$

Substituting in Eqs. (6), (4), and (2), Eq. (22) can be rearranged to

$$\begin{aligned}\Phi_{4a2a} &= \frac{\mu_0 Rl}{g_0}\left(1+\frac{x}{g_0}\cos\phi_s\right)\\ &\quad\cdot\left(\frac{2}{\pi}N_4 i_4 a\cos 2\phi_s+\frac{2}{\pi}N_2 i_{2a}\cos\phi_s-\frac{N_2 i_{2a}}{\pi g_0}\right)\end{aligned} \tag{23}$$

The radial force per unit area generated by the currents in the 2*a* and 4*a* windings can be calculated by means of the Maxwell stress tensor as

$$\begin{aligned}\sigma_{4a2a} &= \frac{B^2_{4a2a}}{2\mu_0}\approx\frac{2\mu_0}{\pi^2 g_0^2}\left(1+\frac{2x}{g_0}\cos\phi_s\right)\\ &\quad\cdot\left[(N_4 i_{4a}\cos 2\phi_s)^2+2N_4 N_2 i_{4a} i_{2a}\cos 2\phi_s\cos\phi_s\right]\end{aligned} \tag{24}$$

Note that in the final expression for σ_{4a2a}, the terms that are proportional to x^2/g_0^2 or $N_2^2 i_{2a}^2$ are ignored. This is because the incremental displacement of the rotor is usually small compared to the nominal air-gap length, and thus, the second-order terms for x/g_0 are neglected here. Also, the ampere-turns of the suspension windings $N_2 i_{2a}$ are usually about ten times smaller than that of the motor windings $N_4 i_{4a}$, and thus, the magnetic force generated by the suspension winding alone is neglected.

There are then two remaining terms left in the last bracket in Eq. (24). They are the stress generated by the four-pole motor field only and the stress generated by the interaction between the four-pole field and the two-pole field. The first term corresponds to the destabilizing radial force generated by the 4*a* winding, as discussed in Sec. 3.3. The second term corresponds to the suspension control forces, which are generated by the interactions between the motor field and suspension field. Define the suspension stress part of Eq. (24) as σ^s_{2a4a}. Integrating it over the air gap, the suspension control force acting on the rotor in the positive x-direction can be calculated as

$$f_x^s = \int_0^{2\pi} RlF^s_{2a4a}\cos\phi_s\mathrm{d}\phi_s = \frac{2\mu_0 RlN_4 N_2 i_{4a}}{\pi g_0^2}i_{2a} \tag{25}$$

The suspension forces generated by the coupling of other windings can be calculated by the same approach. With the four-pole windings excited with symmetrical AC currents specified in Eq. (16), we can express the suspension forces in matrix form as

$$\begin{bmatrix} f_x^s \\ f_y^s \end{bmatrix} = \frac{2\mu_0 RlN_4N_2I_4}{\pi g_0^2} \begin{bmatrix} \cos 2\theta & \sin 2\theta \\ \sin 2\theta & -\cos 2\theta \end{bmatrix} \begin{bmatrix} i_{2a} \\ i_{2b} \end{bmatrix} \tag{26}$$

Note again that in this derivation, only the magnetic reluctance forces due to the coupling of the four-pole and two-pole field are considered, and the effect of the rotor's magnetic field, rotor eccentricity, and the force generated by the two-pole field only are neglected. It can be seen that the calculated suspension forces are linear with respect to the suspension control currents, and they do not depend on the rotor's eccentric displacements. This is due to the *hard linearization* in the magnetic designs. The reluctance force magnetic levitation in a bearingless motor can be viewed as a *flux steering* device, where the suspension control field is steering the motor field in a rotating magnetic field to generate control forces. Readers are referred to Ref. [16] for details about flux steering devices.

In the reluctance force magnetic levitation in a bearingless motor system, the suspension winding currents are usually regarded as the control input signals. Let us define the coefficient in Eq. (26) as the *force constant* of the radial suspension system of a bearingless motor as

$$K_i = \frac{2\mu_0 RlN_4N_2I_4}{\pi g_0^2} \tag{27}$$

3.5 Transfer Function. In this section, a transfer function model of the reluctance force radial suspension in a bearingless motor is derived. Without loss of generality, in this analysis let us consider the magnetic levitation in the x-direction at a time instant that the stator field angle $\theta = 0$, and the rotor's radial eccentric displacement is in the x-direction. The four-pole motor currents at this instance are $i_{4a} = I_4$ and $i_{4b} = 0$, and the rotor's radial displacements in the x- and y-directions are $x = s$ and $y = 0$, respectively. The unstable radial force generated by the four-pole motor windings can then be written as $f^m = K_s x$, and the suspension force in the x-direction is $f^s = K_i i_{2a}$. Define the rotor mass as m. The mechanical dynamic equation of the rotor along the x-direction at the vicinity of the center can then be written as

$$m\frac{\mathrm{d}^2 x}{\mathrm{d}t} = K_i i_{2a} + K_s x \tag{28}$$

By rearranging and taking the Laplace transform of Eq. (28), a transfer function model from the suspension winding current i_{2a} to the rotor displacement x can be derived as

$$\frac{X(s)}{I_{2a}(s)} = \frac{K_i}{ms^2 - K_s} \tag{29}$$

Note the negative sign in front of K_s in this result. This transfer function is consistent with the dynamics of a single degree-of-freedom magnetic levitation system, where an unstable pole exists in the suspension dynamics due to the negative stiffness.

Although in this analysis only the x-direction is considered, we can use a rotational transformation to generalize the above analysis to any radial direction. This model can also be applied to three-phase AC motors via the Clarke transformation to transfer between two-phase and three-phase systems. Note that a coefficient of $\sqrt{3}/\sqrt{2}$ needs to be added to all current amplitudes due to the Clarke transformation. For a commonly used three-phase bearingless motor, the negative stiffness and the force constant values in Eq. (29) become

$$K_s = \frac{3}{\pi}\frac{\mu_0 RlN_4^2}{g_0^3} I_m^2 \ \text{(N/m)} \tag{30}$$

$$K_i = \frac{\sqrt{6}}{\pi}\frac{\mu_0 RlN_2N_4}{g_0^2} I_m \ \text{(N/A)} \tag{31}$$

where I_m is the zero-to-peak current amplitude in the three-phase motor windings.

4 Experimental Validations

4.1 Experimental Setup. A bearingless motor in an one-axis magnetically suspended reaction sphere (1D-MSRS) is being used to test the suspension system dynamics. Figure 5 shows the

(*a*) (*b*)

Fig. 5 Photograph of the experimental hardware for the bearingless motor 1D-MSRS: (*a*) structure and (*b*) stator and rotor

photographs of the experimental setup. Readers are referred to Ref. [9] for a detailed description of the system. The motor drive in the 1D-MSRS is a hybrid hysteresis–induction motor, whose rotor is made of a piece of solid, conductive, and magnetically hard D2 steel. When the motor is running in asynchronous mode, the eddy current inside the rotor is a major torque generation means, and the motor demonstrates hysteresis and induction motor behavior. The motor can also perform synchronous operation, and in this operation mode, the hysteresis effect of the rotor is the only source of torque generation.

The stator of the 1D-MSRS has 24 slots. Two sets of three-phase windings with four-pole and two-pole configurations, respectively, are arranged in the stator slots, where the four-pole windings are the motor windings, and the two-pole windings are the suspension windings. Table 1 presents the design parameters of the bearingless motor system in the 1D-MSRS. In this system, the spherical rotor diameter is much larger than the stator length, and the torque and suspension force generations are assumed as only generated on the rotor surface that is engaged with the stator. That is, the bearingless motor in the 1D-MSRS is approximated as a cylindrical rotor bearingless motor of length equal to the stator length.

The suspension force generation in the bearingless motor in the 1D-MSRS is achieved by means of magnetic reluctance forces. In the 1D-MSRS, the induced rotor magnetic field on the sphere surface is approximately ten times weaker compared to the stator field, and thus, the effects of rotor field on the suspension force generation are neglected.

4.2 Test Results.

The modeled system dynamics is presented first. Substituting the parameters in Table 1 into the transfer function model given in Eqs. (29)–(31) yields the modeled plant Bode plot of the bearingless motor system in 1D-MSRS shown in Fig. 6. Note that the break frequency and the direct current (DC) gain of the system Bode plot vary with the motor winding current amplitude, while the phase of the system remains -180 deg for all frequencies due to the negative stiffness.

Table 1 Design parameters for bearingless motor in 1D-MSRS

Parameter	Value
Rotor radius	27 mm
Stator length	10 mm
Rotor mass	0.63 kg
Air-gap length between stator and rotor	0.5 mm
Number of slots on stator	24
Number of phase for motor winding	3
Number of poles for motor winding	4
Number of turns per slot for motor winding	80
Number of phase for suspension winding	3
Number of poles for suspension winding	2
Number of turns per slot for suspension winding	40

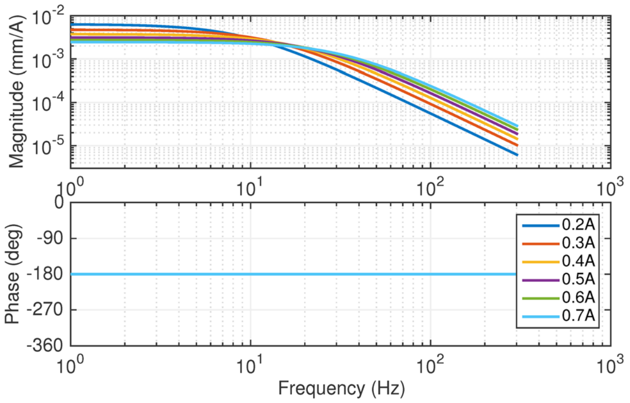

Fig. 6 Modeled plant frequency response for the x-directional suspension of bearingless motor in 1D-MSRS under different motor winding current amplitudes I_m (zero-to-peak)

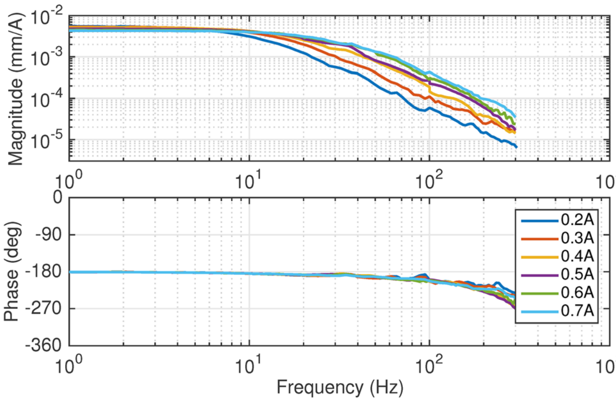

Fig. 7 Experimentally measured plant frequency response for x-direction rotor suspension from the equivalent two-phase suspension control current i_{2a} (A) to the x-directional rotor displacement x (m) under different three-phase four-pole excitation amplitudes I_m (zero-to-peak)

The dynamics of the bearingless motor are measured and are compared with the modeled dynamics. The x-directional rotor suspension system dynamics in the 1D-MSRS are being measured under different four-pole winding current amplitude values, with the two-phase, two-pole current amplitude in the stationary coordinate being the input, and the x-directional rotor displacement being the output. The measurements are taken when the motor is under synchronous operation at 1800 rpm. Note that this measurement must be carried out with the feedback control loop closed since the open-loop system is unstable. The measured Bode plot is presented in Fig. 7. It is consistent with the modeled dynamics shown in Fig. 6, where the system dynamics becoming faster as the motor winding current I_m is increased.

Figure 8 plots the break frequencies of the modeled and measured plant frequency responses with respect to the motor winding current amplitude I_m. The break frequency of the plant Bode plot is nearly linear with the motor winding excitation current I_m, and the modeled break frequency data well match the experimental measured data. This change of the break frequency also implies that the reluctance force magnetic suspension in a bearingless motor requires a minimum driving current amplitude in the motor windings, even when no driving torque is needed, in order to maintain radial suspension.

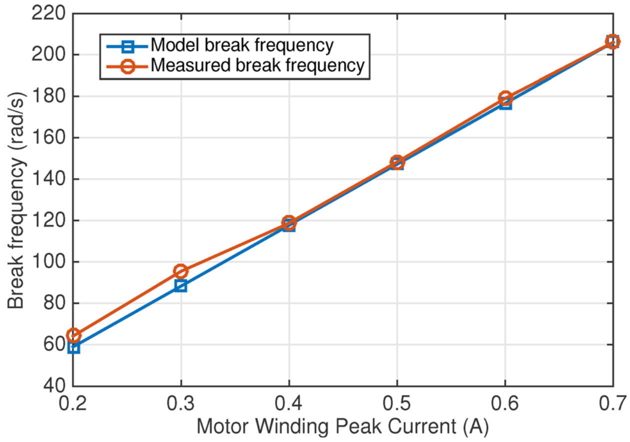

Fig. 8 Modeled and measured break frequencies of plant Bode plot with varying driving current amplitudes

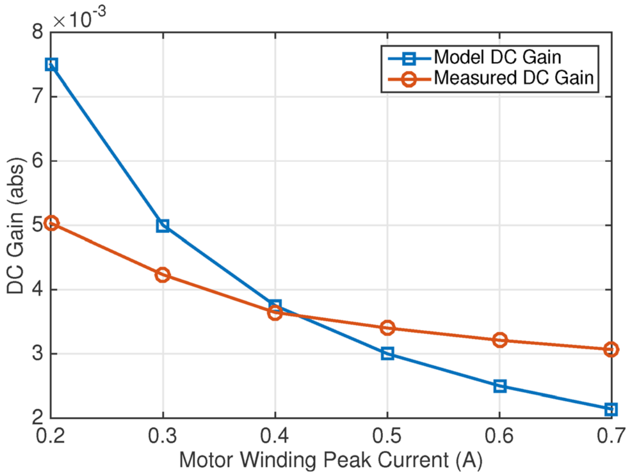

Fig. 9 Modeled and measured DC gain of plant Bode plot with different driving current amplitudes

Figure 9 shows the DC gains of the modeled and measured plant frequency responses of the bearingless motor suspension system. It shows that in terms of the DC gain, the variation trend of the model and the measurement is consistent, but the data are not aligned as well, in that the model has a larger variation of the DC gain. To our understanding, this is because in the experiment when the motor winding current value is relatively low, the assumption of motor winding ampere-turns is way larger than that of the suspension winding no longer holds. To correct this deviation will require including the radial forces generated by the suspension windings themselves, which leads to a nonlinear model. In this work, this error is accepted since it does not prevent us from using the model for system prediction and linear controller design.

5 Suspension Control

This section discusses the suspension controller design of the bearingless motor. Figure 10 shows a block diagram of the reluctance force magnetic suspension control for a bearingless motor. The four-pole motor windings are excited with symmetrical three-phase AC currents. The rotor radial displacements in the *x*- and *y*-direction are detected by two displacement sensors and compared with their reference values. The error signals are then amplified by the independent proportional–integral–derivative (PID) controllers to generate the control effort signals u_x and u_y, and these commands are transformed into the rotating three-phase coordinates through Park and Clarke transformations, and are then amplified into the two-pole suspension winding current values. The Park transformation in Fig. 10 uses the stator field angle as the transformation angle, which aligns the suspension control field with the motor field. This treatment is based on the assumption that the magnetic field due to the rotor's magnetization is small compared with the stator field, and thus, the reluctance forces are the main suspension control force generation mechanism.

In many applications, the motor winding currents of a bearingless motor need to adjust according to the motor torque requirement. Since the plant dynamics of the bearingless motor depend on the motor winding current level, the controllers need to be able to stabilize the system under all excitation conditions. In order to enhance the stable suspension capability of the bearingless motor, the suspension controllers with varying PID controller gains are designed based on the analytical model presented in this paper. The transfer function of the lead–lag form PID controller can be written as

$$C(s) = K_p\left(1+\frac{1}{T_i s}\right)\cdot\frac{\alpha\tau s+1}{\tau s+1} \qquad (32)$$

where K_p is the proportional gain; T_i is the integral time, which determines the zero position of the lag compensator; α is the separation ratio of the lead compensator; and τ is the time constant that determines the pole and zero locations in the lead compensator.

In the design of the controller, we choose loop crossover at β times the plant break frequency, with a fixed phase margin of ϕ_m. Hence under certain excitation amplitude I_m, the desired crossover frequency is $\omega_c = \beta \times 2\pi \times f_{\mathrm{break}}$, where f_{break} is varying with the excitation condition I_m. The phase peak of the lead compensator is placed at the desired crossover frequency; therefore, τ need to adjust by $\tau = 1/\sqrt{\alpha}\omega_c$. The zero position of the lag compensator $1/T_i$ is selected at one decade below the desired crossover frequency. The controller gain K_p is selected to make the loop crossover at the desired frequency. As a result, three parameters in the controller, K_p, τ, and T_i, are adjusted in real-time as a function of the excitation amplitude I_m. This approach has operated successfully in the experiments.

The aforesaid controller design was implemented and tested with the bearingless motor in the 1D-MSRS. In this experiment, we selected $\alpha = 10$ and $\beta = 3$, and the target phase margin is $\phi_m = 40\,\mathrm{deg}$. The loop return ratios of the magnetic suspension system are measured under different motor winding current amplitudes, which is achieved by measuring the frequency response

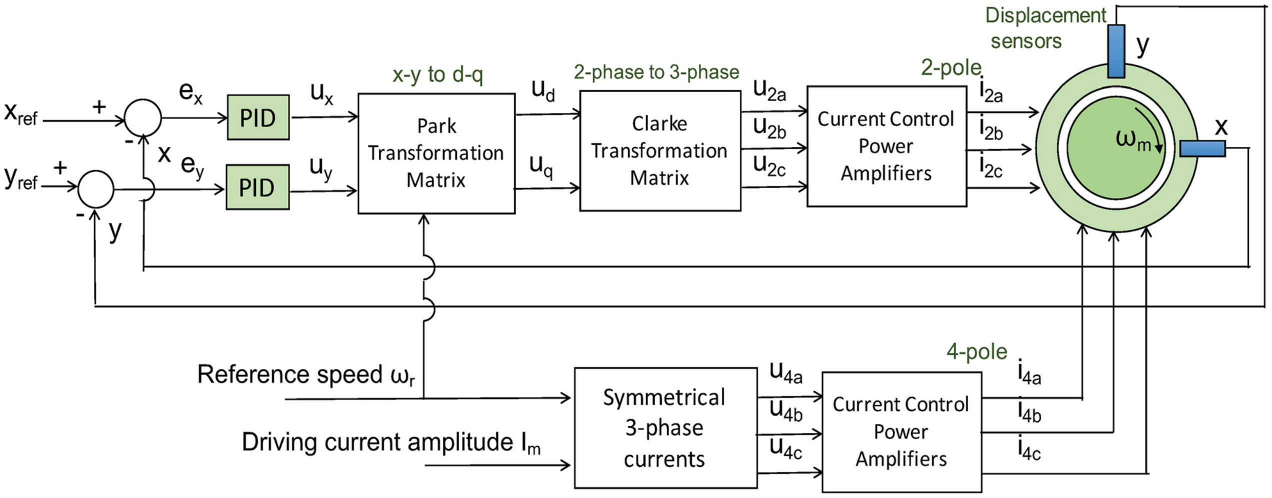

Fig. 10 Block diagram of the reluctance force magnetic suspension control system for the bearingless motor

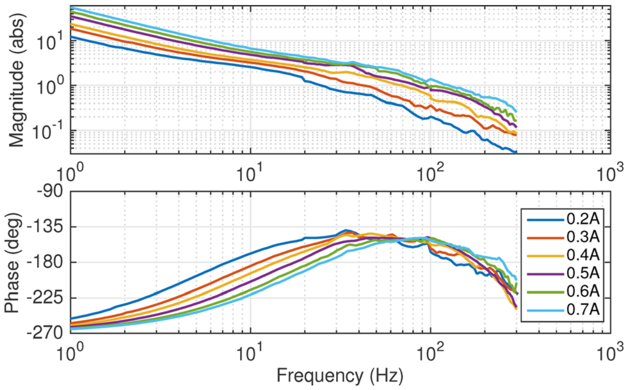

Fig. 11 Measured loop return ratio of the radial suspension in the testing bearingless motor

from the x-directional position error signal (e_x in Fig. 10) to the x-directional rotor position (x in Fig. 10), and the data are shown in Fig. 11. It can be seen from the measured data that the proposed controller design can stabilize the lateral suspension control under different motor current amplitudes. With this controller design, the loop reached a bandwidth varying with the excitation current amplitude and a fixed phase margin of approximately 40 deg. Under 0.2 A excitation current, the loop has a crossover frequency of 150 rad/s. With 0.7 A excitation, the crossover frequency is 620 rad/s. In this way, the radial position of the bearingless motor is successfully regulated at the center of the stator under changing motor excitation amplitudes.

6 Conclusion

In this paper, an analytical dynamic model of the reluctance force magnetic suspension in bearingless motors was derived based on the fundamental electromagnetics. A transfer function model of the system is derived, which provides an effective basis for the loop-shaping control design for the bearingless motor systems with varying motor currents. Measurements with a hybrid hysteresis–induction type bearingless motor are used to validate the model. A suspension controller design approach based on the model is proposed and tested, and the results show that this controller design can effectively maintain the stable suspension operation of the bearingless motor under varying motor current levels.

Acknowledgment

This work was supported by Lincoln Laboratory of M.I.T. via the Advanced Concept Committee. The authors thank National Instruments for contributing the real-time controller.

References

[1] Ooshima, M., and Takeuchi, C., 2011, "Magnetic Suspension Performance of a Bearingless Brushless DC Motor for Small Liquid Pumps," IEEE Trans. Ind. Appl., **47**(1), pp. 72–78.
[2] Grabner, H., Amrhein, W., Silber, S., and Gruber, W., 2010, "Nonlinear Feedback Control of a Bearingless Brushless DC Motor," IEEE/ASME Trans. Mechatronics, **15**(1), pp. 40–47.
[3] Oshima, M., Miyazawa, S., Deido, T., Chiba, A., Nakamura, F., and Fukao, T., 1996, "Characteristics of a Permanent Magnet Type Bearingless Motor," IEEE Trans. Ind. Appl., **32**(2), pp. 363–370.
[4] Amrhein, W., Silber, S., Nenninger, K., Trauner, G., Reisinger, M., and Schoeb, R., 2003, "Developments on Bearingless Drive Technology," JSME Int. J. Ser. C, **46**(2), pp. 343–348.
[5] Okada, Y., Miyamoto, S., and Ohishi, T., 1996, "Levitation and Torque Control of Internal Permanent Magnet Type Bearingless Motor," IEEE Trans. Control Syst. Technol., **4**(5), pp. 565–571.
[6] Chiba, A., Power, D., and Rahman, M., 1991, "Characteristics of a Bearingless Induction Motor," IEEE Trans. Magn., **27**(6), pp. 5199–5201.
[7] Takemoto, M., Suzuki, H., Chiba, A., Fukao, T., and Azizur Rahman, M., 2001, "Improved Analysis of a Bearingless Switched Reluctance Motor," IEEE Trans. Ind. Appl., **37**(1), pp. 26–34.
[8] Imani Nejad, M., 2013, "Self-Bearing Motor Design & Control," Ph.D. thesis, Mechanical Engineering, Massachusetts Institute of Technology, Cambridge, MA.
[9] Zhou, L., 2014, "Magnetically Suspended Reaction Sphere With One-Axis Hysteresis Drive," Master's thesis, Mechanical Engineering, Massachusetts Institute of Technology, Cambridge, MA.
[10] Gieras, J. F., and Saari, J., 2012, "Performance Calculation for a High-Speed Solid-Rotor Induction Motor," IEEE Trans. Ind. Electron., **59**(6), pp. 2689–2700.
[11] Chiba, A., Power, D. T., and Rahman, M., 1995, "Analysis of No-Load Characteristics of a Bearingless Induction Motor," IEEE Trans. Ind. Appl., **31**(1), pp. 77–83.
[12] Chiba, A., Fukao, T., Ichikawa, O., Oshima, M., Takemoto, M., and Dorrell, D. G., 2005, *Magnetic Bearings and Bearingless Drives*, Elsevier, Oxford, UK.
[13] Chiba, A., Deido, T., Fukao, T., and Rahman, M. A., 1994, "An Analysis of Bearingless AC Motors," IEEE Trans. Energy Convers., **9**(1), pp. 61–68.
[14] Baoguo, W., and Fengxiang, W., 2001, "Modeling and Analysis of Levitation Force Considering Air-Gap Eccentricity in a Bearingless Induction Motor," Fifth International Conference on Electrical Machines and Systems, IEEE, New York, Aug. 18–20, Vol. 2, pp. 934–937.
[15] Yikang, H., and Heng, N., 2003, "Analytical Model and Feedback Control of the Levitation Force for an Induction-Type Bearingless Motor," Fifth International Conference on Power Electronics and Drive Systems, IEEE, New York, Nov. 17–20, Vol. 1, pp. 242–246.
[16] Lu, X., et al., 2005, "Electromagnetically-Driven Ultra-Fast Tool Servos for Diamond Turning," Ph.D. thesis, Mechanical Engineering, Massachusetts Institute of Technology, Cambridge, MA.
[17] Fitzgerald, A. E., Kingsley, C., Umans, S. D., and James, B., 2003, *Electric Machinery*, Vol. 5, McGraw-Hill, New York.